

Symmetry-broken self-interstitial defects in chromium, molybdenum, and tungsten

Pui-Wai Ma*

UK Atomic Energy Authority, Culham Science Centre, Oxfordshire OX14 3DB, United Kingdom

S. L. Dudarev†

UK Atomic Energy Authority, Culham Science Centre, Oxfordshire OX14 3DB, United Kingdom
and Department of Materials, University of Oxford, Parks Road, Oxford OX1 3PH, United Kingdom

(Received 21 January 2019; published 24 April 2019)

For several decades, the striking contradiction between the Huang diffuse scattering experiments, resistivity recovery data, and predictions derived from density functional theory (DFT) remained one of the mysteries of defect physics in molybdenum. Since the 1970s, observations of Huang x-ray diffuse scattering appeared to indicate that a self-interstitial atom (SIA) defect in Mo adopts a $\langle 110 \rangle$ dumbbell configuration. However, the low temperature defect diffusion data supported the DFT prediction of a different, highly mobile $\langle 111 \rangle$ SIA defect structure in the same metal. Using DFT simulations, we show that an SIA adopts a symmetry-broken configuration in all the group 6 metals: chromium, molybdenum, and tungsten. The symmetry-broken defect structure, a $\langle 11\xi \rangle$ dumbbell, where ξ is an irrational number, agrees with nudged elastic band analyses of $\langle 110 \rangle$ to $\langle 111 \rangle$ transformations. Direct simulations of Huang diffuse scattering by symmetry-broken defect configurations predicted by DFT explain why no zero intensity lines were observed in experiment and resolve the long outstanding question about the structure of defects in Mo and similar metals. A $\langle 11\xi \rangle$ defect migrates *on average* one dimensionally through a sequence of three-dimensional nonplanar $[11\xi]$ to $[\xi 11]$ or $[1\xi 1]$ transitions. Barriers for defect migration in nonmagnetic Cr, antiferromagnetic Cr, Mo, and W derived from DFT calculations, 0.052, 0.075, 0.064, and 0.040 eV are well correlated with the onset of defect migration temperatures observed experimentally.

DOI: [10.1103/PhysRevMaterials.3.043606](https://doi.org/10.1103/PhysRevMaterials.3.043606)

I. INTRODUCTION

The group 6 metals chromium, molybdenum, and tungsten are elements of profound technological significance. Cr is an indispensable component of stainless steels, preventing corrosion through passivation. It also improves the resistance to swelling of ferritic-martensitic steels exposed to irradiation [1]. Mo, W, and their alloys are refractory metals with high melting points, mechanically stable at high temperature. They are used in a variety of high temperature applications [2,3], for example Mo-25%Re alloys are materials for rocket engine components [4]. Tungsten is a candidate material for divertor and plasma-facing components of a fusion power plant [5,6].

Mechanical properties of metals depend on their microstructure [7]. To model how the microstructure of Cr, Mo, W, and their alloys evolves under irradiation, it is essential to know the structure and thermally activated mobility parameters of self-interstitial atom (SIA) defects. Huang scattering experiments [8–10] appear to show that an SIA in Mo adopts a $\langle 110 \rangle$ configuration, consistent with the diffuse scattering pattern produced by a field of atomic displacements with orthorhombic symmetry. However, this is at odds with density function theory (DFT) predictions that SIA defects in all the body-centered cubic transition metals, with the exception of

ferromagnetic iron, adopt straight linear $\langle 111 \rangle$ dumbbell or crowdion configurations [11–13].

According to the resistivity recovery experiments on electron irradiated materials [14,15], the temperatures T_m^{SIA} of the onset of long range migration of SIA defects in Cr, Mo, and W are 40, 35, and 27 K, respectively. In many other bcc transition metals T_m^{SIA} is below 6 K, which is the lowest temperature accessible to observations. If one assumes that a defect adopts a $\langle 110 \rangle$ configuration then, irrespectively of whether its migration follows a three-dimensional translation-rotation pathway [16] or a two-dimensional pathway [17] (Fig. 1), in comparison with iron where $T_m^{\text{SIA}} = 120$ K, the experimentally observed values of T_m^{SIA} in group 6 metals are too low. On the other hand, if an SIA adopted a linear $\langle 111 \rangle$ configuration and diffused one dimensionally [18], the corresponding temperatures T_m^{SIA} would be significantly lower than what is observed experimentally.

Fitzgerald and Nguyen-Manh [18] argued that the relatively high values of T_m^{SIA} in group 6 elements were a consequence of the double peak structure of the $\langle 111 \rangle$ interatomic-string potential, affecting the Peierls barrier for the motion of SIA defects. The argument was based on solutions of a constrained one-dimensional Frenkel-Kontorova model, parametrized using DFT calculations. However, the study involved no direct DFT analysis of SIA migration barriers or possible deviations from purely one-dimensional diffusion.

A recent direct DFT nudged elastic band (NEB) study showed that the barrier for one-dimensional diffusion of a

*leo.ma@ukaea.uk

†sergei.dudarev@ukaea.uk

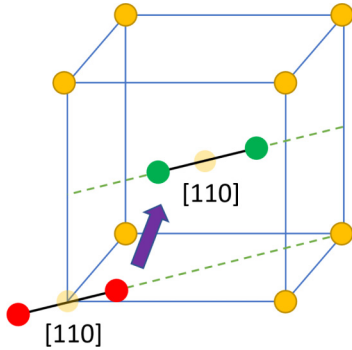


FIG. 1. Sketch illustrating a two-dimensional transition pathway of migration of a $\langle 110 \rangle$ dumbbell proposed by Jacques and Robrock [17].

$\langle 111 \rangle$ SIA dumbbell defect in tungsten was just 2 meV [19], and that it had a simple single-peak structure. A straight $\langle 111 \rangle$ dumbbell moves from one equilibrium position to another via a $\langle 111 \rangle$ crowdion saddle point configuration. In a classical transition state theory approximation [20] the barrier of 2 meV corresponds to the temperature of onset of SIA migration of 0.7 K, as detailed in Sec. IV below. Quantum transition state theory [19] that takes zero-order atomic vibrations into account, predicts that defects diffuse at even lower temperature. Neither classical nor quantum predictions agree with experimental observations, and this is unusual given that DFT calculations normally match experimental data fairly well [16].

Can an SIA defect adopt neither a straight $\langle 111 \rangle$ nor a $\langle 110 \rangle$ configuration? Olsson [21] noted that the energy of a $\langle 221 \rangle$ dumbbell in Cr was lower than the energy of either $\langle 111 \rangle$ or $\langle 110 \rangle$ defect structures. Han *et al.* [22] also found that the energy of a canted $\langle 111 \rangle$ dumbbell in Mo, computed using a relatively small cell, was slightly lower than that of a straight $\langle 111 \rangle$ configuration. Ventelon *et al.* [23] noted that self-interstitial defects in Cr, Mo, and W might adopt structures different from a straight $\langle 111 \rangle$ configuration. They

TABLE I. Elastic constants (in GPa units) evaluated using the Le Page and Saxe [35] method for a two-atom cell and $30 \times 30 \times 30$ k -point mesh. Ω_0 (\AA^3) and a_0 (\AA) are the atomic volume and the lattice constant, respectively. Calculations were performed using the GGA-PBE exchange-correlation functional assuming nonmagnetic (NM) or collinear antiferromagnetic (AFM) states of Cr, and nonmagnetic states of Mo and W. Experimental lattice constants are taken from Ref. [36], elastic constants for Cr are from Ref. [37], and for Mo and W are from Ref. [38].

PBE	C_{11}	C_{12}	C_{44}	Ω_0	a_0
Cr/AFM	448.12	62.03	102.13	11.72	2.862
Cr/NM	509.67	144.27	105.73	11.49	2.843
Mo	469.07	157.72	99.71	15.77	3.160
W	518.26	199.77	142.09	16.14	3.184
Expt.					
Cr	394.1	88.5	103.75	11.94	2.88
Mo	464.7	161.5	108.9	15.63	3.15
W	522.4	204.4	160.6	15.78	3.16

TABLE II. Formation energies E^F of point defects in Cr/AFM, Cr/NM, Mo, and W evaluated using the GGA-PBE exchange-correlation functional. Calculations were performed using simulation cells containing $4 \times 4 \times 4$ bcc unit cells. A $\langle 11\xi \rangle$ dumbbell has the lowest energy among all the SIA configurations explored in this study. Vacancy data are also included for completeness. All the energies are given in eV. The value of parameter ξ depends on the material and, where applicable, on its magnetic structure.

$4 \times 4 \times 4$	Cr/AFM	Cr/NM	Mo	W
$\langle 11\xi \rangle$ d	6.361	6.074	7.399	10.249
$\langle 111 \rangle$ d	6.617	6.247	7.475	10.287
$\langle 111 \rangle$ c	6.555	6.243	7.479	10.289
$\langle 110 \rangle$ d	6.515	6.218	7.580	10.576
Tetra	6.918	6.889	8.358	11.717
$\langle 100 \rangle$ d	7.275	7.256	8.890	12.196
Octa	7.354	7.307	8.916	12.265
Vac	3.004	2.875	2.787	3.223
ξ	0.355	0.405	0.468	0.526

observed that Olsson's earlier result [21] might be a part of a general trend spanning the entire group of the three metals, and investigated the structure of a self-interstitial defect in tungsten. The results were not fully conclusive, and the case of molybdenum did not receive attention. Finally the authors of Ref. [23] concluded in favor of a straight $\langle 111 \rangle$ defect configuration in tungsten. Recently, Gharraee and Erhart [24] found that a lower symmetry mixed self-interstitial defect involving a Ti, V, or Re solute atom in W had lower energy than $\langle 111 \rangle$ or $\langle 110 \rangle$ dumbbells. They termed the resulting structure a bridge interstitial. All the above studies [21,22,24] point to a possible occurrence of a lower symmetry defect configuration in group 6 elements, different from either a simple linear $\langle 111 \rangle$

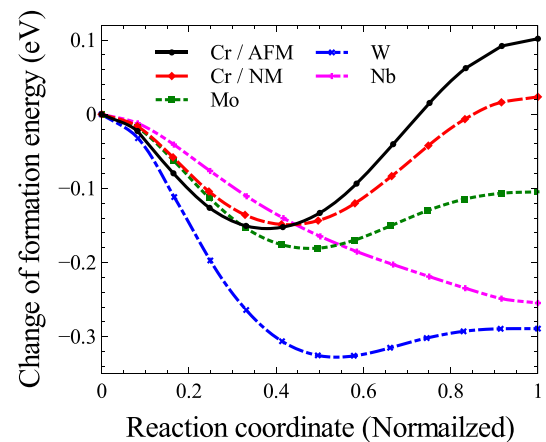


FIG. 2. Results of nudged elastic band calculations illustrating how the formation energy of an SIA dumbbell varies as a function of the orientation of the axis of the defect. The orientation changes from being collinear to the $[110]$ direction (the left edge of the diagram) to being collinear to the $[111]$ direction (the right edge of the diagram). The curves were computed taking into account the elastic correction associated with the use of periodic boundary conditions [13,33,34]. Note that the only curve in the figure that is monotonic refers to Nb, which is a group 5 metal.

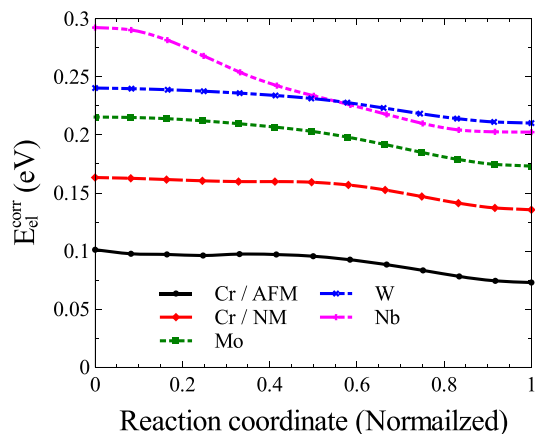


FIG. 3. The elastic correction E_{el}^{corr} part of the formation energy of defects corresponding to the curves shown in Fig. 2.

defect, or a $\langle 110 \rangle$ dumbbell. If this were indeed the case, the mode of migration of the defect would deviate from pure one-dimensional motion that is often assumed in tungsten and other nonmagnetic BCC metals.

Below we resolve the controversy and explain the origin of disagreement between the Huang scattering and resistivity recovery experimental results. We also explain elastic after-effect observations and identify a deficiency associated with earlier DFT calculations of defects in W, Mo, and Cr. We find that a canted $\langle 11\xi \rangle$ SIA configuration, where ξ is an irrational number, represents the lowest energy defect structure in all the metals of group 6 in the periodic table. A migrating defect follows a three-dimensional translation-rotation pathway, where the average trajectory is parallel to a $\langle 111 \rangle$ crystallographic direction. The barriers for migration predicted by DFT

TABLE III. Formation energies of selected point defects in Cr/AFM, Cr/NM, Mo, and W evaluated using a cell containing $5 \times 5 \times 5$ bcc unit cells. A $\langle 11\xi \rangle$ dumbbell still represents the lowest energy configuration in all the three metals.

$5 \times 5 \times 5$	Cr/AFM	Cr/NM	Mo	W
$\langle 11\xi \rangle d$	6.453	5.919	7.448	10.256
$\langle 111 \rangle d$	6.644	6.095	7.519	10.306
$\langle 110 \rangle d$	6.548	6.060	7.628	10.579
ξ	0.356	0.397	0.447	0.482

calculations for all the three metals agree with the observed temperatures of the onset of diffusion of SIA defects.

Using elastic dipole tensors of $\langle 11\xi \rangle$ defects, we simulate Huang diffuse x-ray scattering patterns and find that the features, using which the defect structures were classified in experiments performed in the 1970s [9], are surprisingly similar to those of a $\langle 110 \rangle$ dumbbell, despite the fact that the structures of defects themselves are different. It is this unusual manifestation of symmetry-breaking effect, occurring in a defect structure, that reconciles a number of seemingly contradictory experimental observations, and resolves the inconsistency between experiment and *ab initio* interpretation of data that remained outstanding for several decades.

II. METHODOLOGY

All the *ab initio* calculations were performed using Vienna *ab initio* simulation package (VASP) [25–28] in the generalized gradient approximation (GGA), using the exchange-correlation functional by Perdew, Burke, and Ernzerhof (PBE) [29,30]. Plane wave energy cutoff was set at 450 eV. A

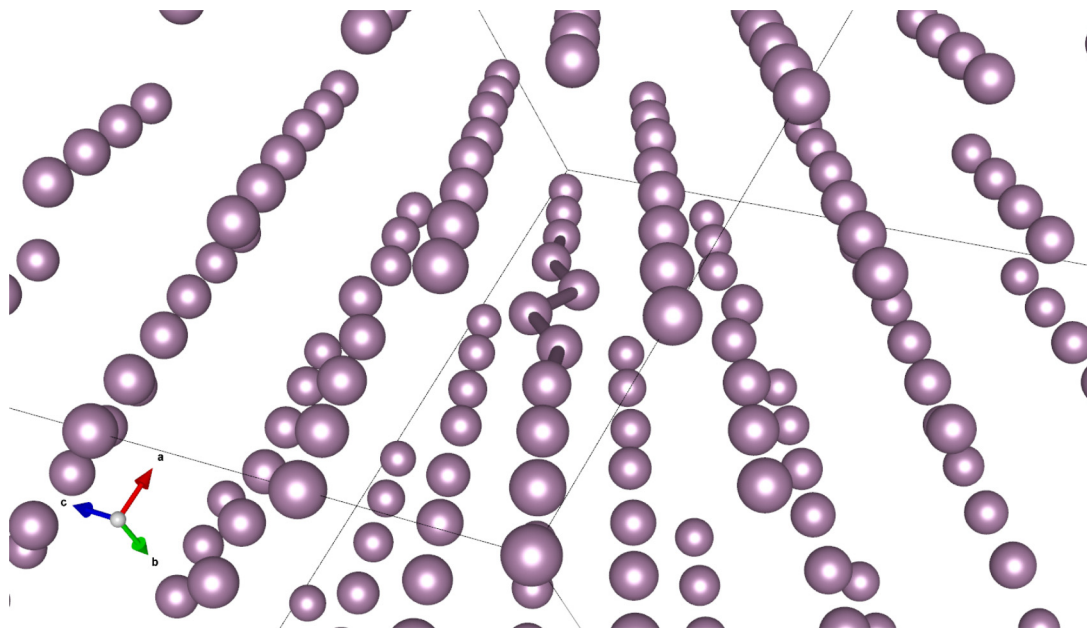


FIG. 4. Atomic structure of a symmetry-broken $\langle 11\xi \rangle$ SIA dumbbell defect in Mo, simulated using a supercell containing $5 \times 5 \times 5$ unit cells. Symmetry breaking in the core of the defect gives rise to buckling of the central $[111]$ atomic string containing an extra atom. Buckling can occur in one of the three $\{1\bar{1}0\}$ atomic planes equivalent by symmetry with respect to the straight linear $\langle 111 \rangle$ configuration of the defect.

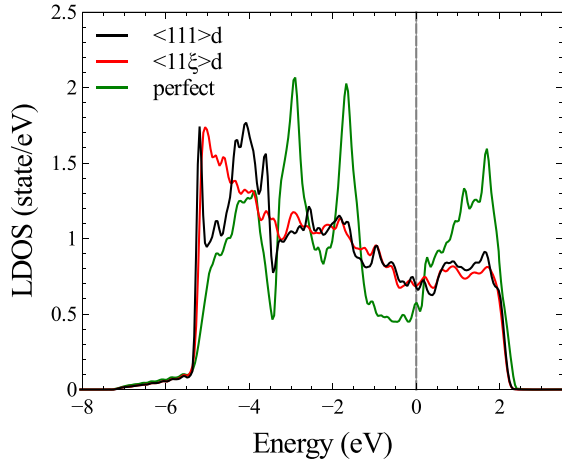


FIG. 5. The local density of states (DOS) for one of the two atoms at the center of $\langle 111 \rangle$ and $\langle 11\xi \rangle$ dumbbell configurations in Mo. A plot showing the DOS computed for perfect bcc lattice is shown for comparison. The position of the Fermi energy for all the three structures corresponds to the origin of the horizontal axis and is indicated by a dashed vertical line.

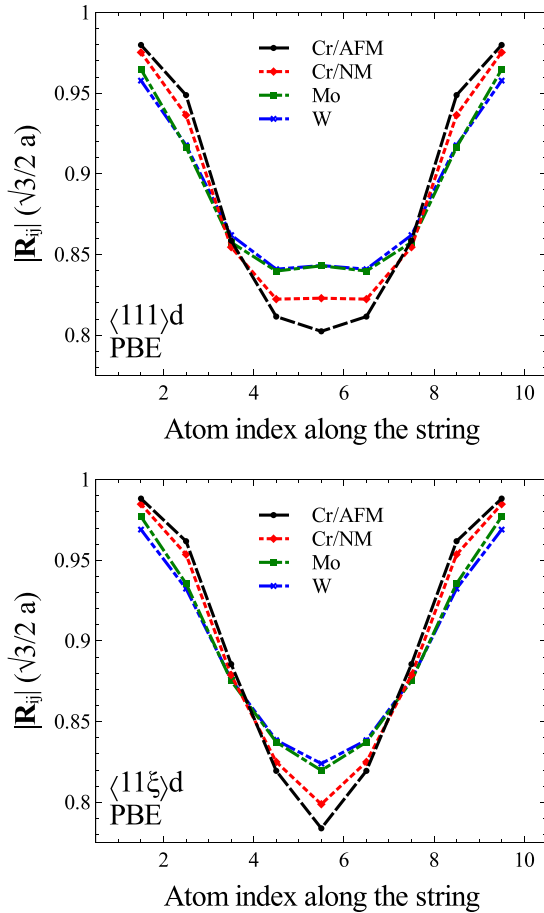


FIG. 6. Distances between successive atoms i and $j = i + 1$ in a $\langle 111 \rangle$ atomic string containing an extra atom. (Top) Data for a $\langle 111 \rangle$ dumbbell and (bottom) data for a $\langle 11\xi \rangle$ configuration in Cr/AFM, Cr/NM, Mo, and W. Positions of atoms were computed using the GGA-PBE functional.

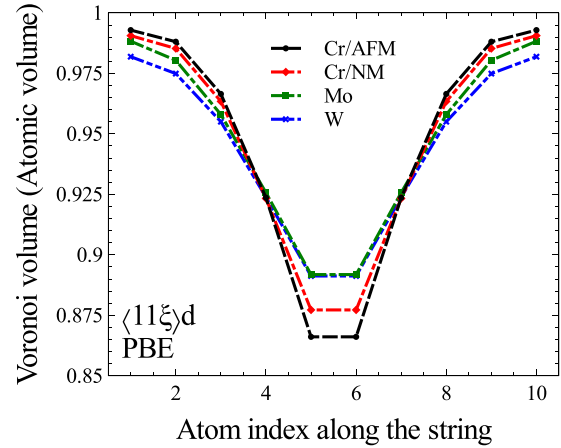
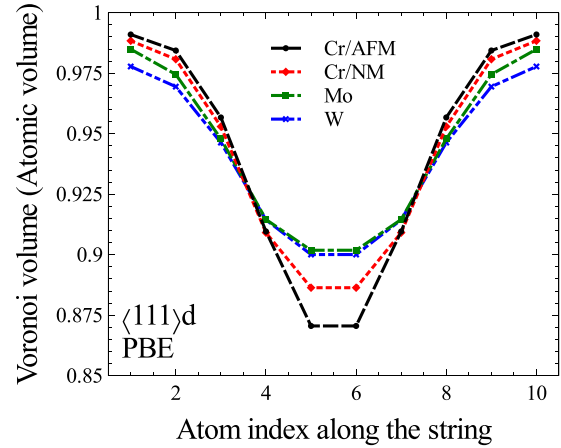


FIG. 7. Voronoi volumes of atoms belonging to a $\langle 111 \rangle$ atomic string containing an extra atom. (Top) Data for a $\langle 111 \rangle$ dumbbell and (bottom) data for a $\langle 11\xi \rangle$ configuration of a defect in Cr/AFM, Cr/NM, Mo, and W. All the calculations were performed using the GGA-PBE functional.

simulation supercell involved $4 \times 4 \times 4$ bcc unit cells. $5 \times 5 \times 5$ k -points mesh was used in all the calculations. To explore the cell size effect, we also performed simulations using a larger supercell containing $5 \times 5 \times 5$ bcc unit cells, with a $4 \times 4 \times 4$ k -points mesh. Reference perfect lattice cells were relaxed to a stress-free condition. While keeping the cell size and shape the same as in the perfect lattice case, simulation cells containing various SIA configurations were created and ionic positions relaxed. The maximum residual force on an atom in a fully relaxed defect configuration was smaller than 1×10^{-3} eV/Å. Semicore shells were treated as valence electrons, and 12 valence electron per atoms were included in every calculation of a defect structure in Cr, Mo, and W to achieve the sufficient accuracy of evaluation of interatomic forces in the highly compressed core region of the defect.

For Mo and W, only nonmagnetic (NM) calculations were performed. For Cr, we performed NM and collinear magnetic calculations. Although the electronic ground state of Cr is believed to have the form of a spin density wave (SDW) [31], a collinear antiferromagnetic (AFM) state was chosen for spin polarized calculations. This AFM state has the energy very close to that of the SDW within the margin of *ab initio*

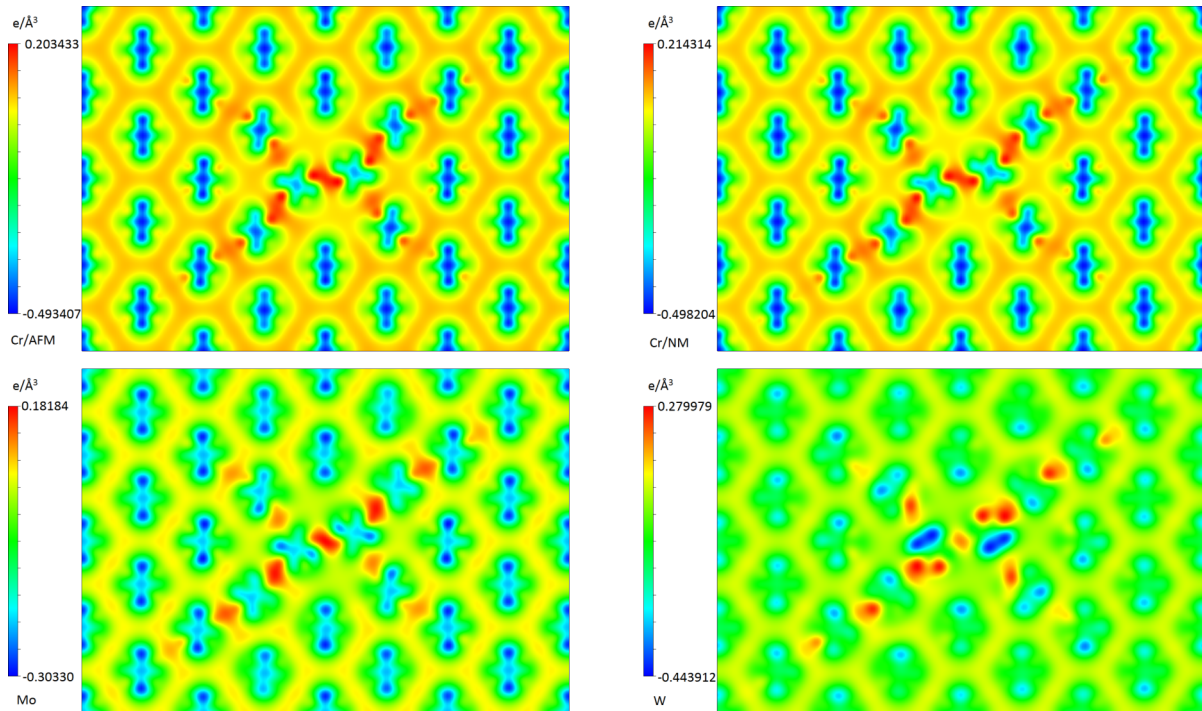


FIG. 8. Two-dimensional plots of electron charge density difference computed for a $\langle 11\bar{1}0 \rangle$ dumbbell configuration in the $(1\bar{1}0)$ plane in Cr/AFM, Cr/NM, Mo, and W. Calculations were performed using the GGA-PBE functional. Electron charge density difference is defined as the self-consistent electron density minus a superposition of atomic charge densities.

calculations [32]. An AFM state was set up by initializing magnetic moments similar to those of a perfect lattice configuration, but with magnitudes set to zero near the highly

compressed core of the defect. The final ground state AFM magnetic structure was determined from a self-consistent electronic structure calculation.

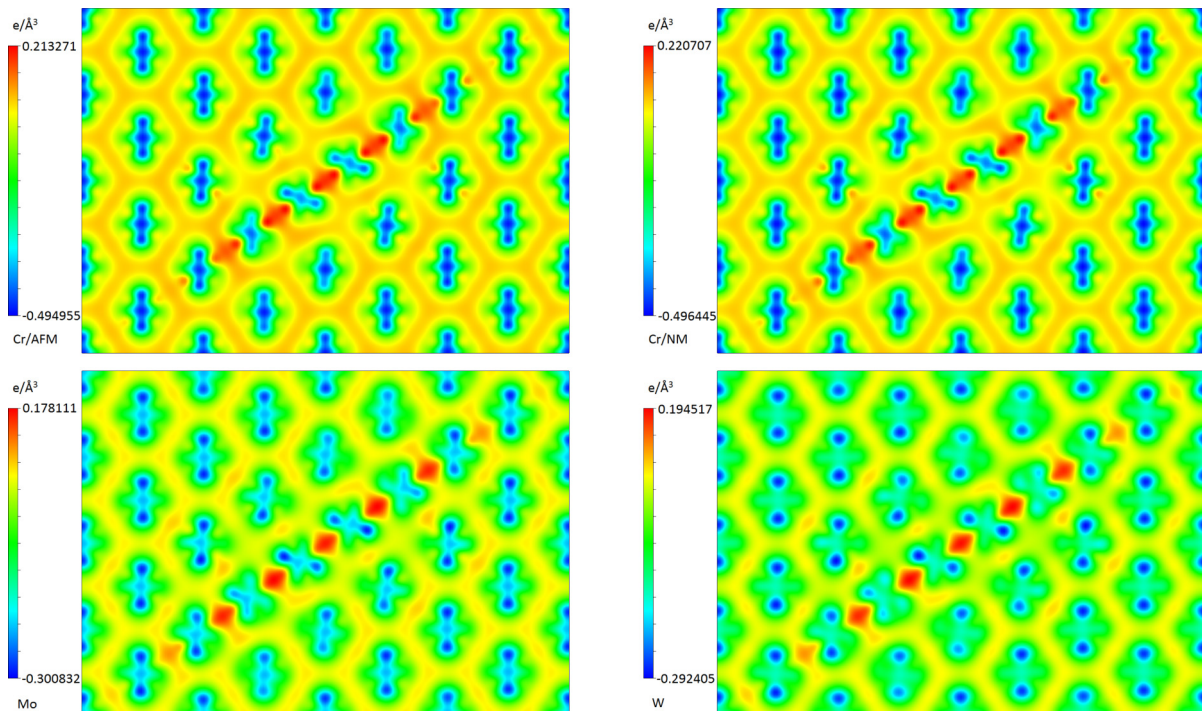


FIG. 9. Two-dimensional plots of electron charge density difference computed for a $\langle 111 \rangle$ dumbbell configuration in the $(1\bar{1}0)$ plane in Cr/AFM, Cr/NM, Mo, and W. Calculations were performed using the GGA-PBE functional. Electron charge density difference is defined as the self-consistent electron density minus a superposition of atomic charge densities.

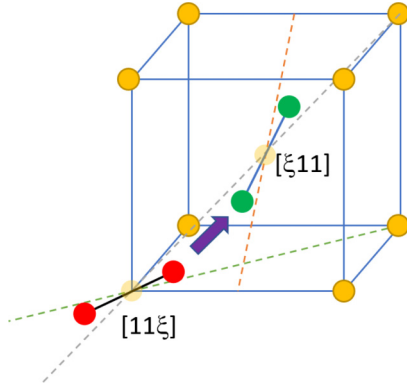


FIG. 10. Schematic diagram illustrating the migration pathway of an SIA defect from a $[11\xi]$ to a $[\xi11]$ dumbbell configuration. Values of parameter ξ for group 6 metals are listed in Tables II and III. Note that the initial and final configurations of the defect are associated with symmetry breaking occurring in two *different* $\{110\}$ planes.

The formation energy of a defect is

$$E^F = E_{\text{def}}(N_{\text{def}}) - \frac{N_{\text{def}}}{N_{\text{bulk}}} E_{\text{bulk}}(N_{\text{bulk}}) - E_{\text{el}}^{\text{corr}}, \quad (1)$$

where N_{bulk} and N_{def} are the numbers of atoms in a reference cell and in a cell containing a defect, E_{def} is the total energy of the cell containing a defect, E_{bulk} is the energy of the reference cell, and $E_{\text{el}}^{\text{corr}}$ is the elastic correction energy that needs to be included given that calculations were performed using periodic boundary conditions. Further detail are given in Refs. [13,33,34]. Elastic constant tensors C_{ijkl} involved in the evaluation of $E_{\text{el}}^{\text{corr}}$ were computed using the Le Page and Saxe method [35] for a two atom simulation cell and a $30 \times 30 \times 30$ k -point mesh. The computed elastic constants are given in Table I.

Migration energy E^M of a defect was computed using the NEB method [39,40], where E^M is defined as the maximum

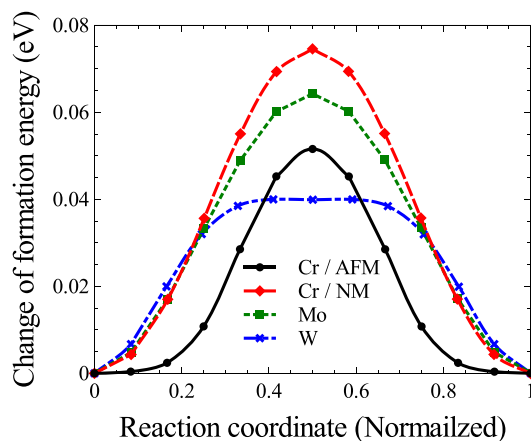


FIG. 11. Migration energy barriers computed using the nudged elastic band method, and corresponding to the trajectory of migration of a symmetry-broken $[11\xi]$ SIA dumbbell to an adjacent cell, as illustrated in Fig. 10. Calculations were performed using the GGA-PBE exchange-correlation functional.

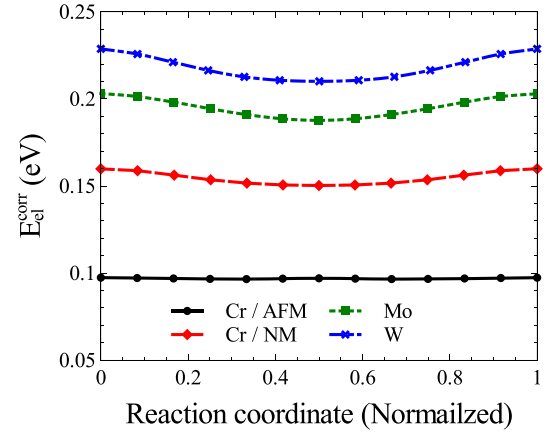


FIG. 12. Energy contribution due to the elastic correction $E_{\text{el}}^{\text{corr}}$ corresponding to the trajectory of migration shown in Figs. 10 and 11.

variation of the formation energy along a transition pathway linking two equilibrium configurations. Each NEB calculation involved 11 images, where the residual force on an atom in each image was lower than 0.01 eV/\AA . At each point on a transition pathway the formation energy of a defect was corrected for the elastic effects associated with the use of periodic boundary conditions [13,33,34].

III. FORMATION ENERGY OF SIA DEFECTS IN Cr, Mo, AND W

DFT calculations of various SIA configurations were performed using a simulation cell containing $4 \times 4 \times 4$ bcc unit cells. The defect configurations included in the study were $\langle 111 \rangle$ dumbbell, $\langle 111 \rangle$ crowdion, $\langle 110 \rangle$ dumbbell, tetrahedral site interstitial, $\langle 100 \rangle$ dumbbell, and an octahedral site interstitial. For completeness we have also computed the formation energy of a monovacancy. The formation energies of defects are given in Table II. Calculations show that the formation energies of a $\langle 110 \rangle$ dumbbell, $\langle 111 \rangle$ dumbbell, and $\langle 111 \rangle$ crowdion are similar. These results are compatible with previous DFT studies [11,12,21,41] showing that a $\langle 110 \rangle$ dumbbell has lower energy in Cr, whereas a $\langle 111 \rangle$ dumbbell has lower energy in Mo and W.

Bearing in mind studies by Olsson [21], Han *et al.* [22], and Gharaee and Erhart [24], we have also explored if there were an even more stable SIA configuration, intermediate between a $\langle 110 \rangle$ dumbbell and a $\langle 111 \rangle$ dumbbell. To

TABLE IV. Barriers for defect migration in group 6 metals, the estimated transition state theory onset of migration temperatures, and the onset of migration temperatures observed in electron irradiated metals using the resistivity recovery technique [14].

Metal	E^m (eV)	Est. T_m (K)	Expt. T_m (K)
Cr/AFM	0.052	18.7	40
Cr/NM	0.075	27.0	40
Mo	0.064	23.5	35
W	0.040	14.7	27

TABLE V. Elements of dipole tensor P_{ij} (in eV units) and parameters π_1 , π_2 , and π_3 computed for $\langle 11\xi \rangle$, $\langle 111 \rangle$, and $\langle 110 \rangle$ dumbbells in Cr/AFM. *Ab initio* calculations were performed using simulation cells containing $4 \times 4 \times 4$ bcc unit cells.

Cr/AFM	P_{11}	P_{22}	P_{33}	P_{12}	P_{23}	P_{31}	π_1	π_2	π_3	π_2/π_1	π_3/π_1
$\langle 11\xi \rangle$ d	18.389	18.389	21.882	4.040	2.058	2.058	1147.0	4.067	16.528	0.00355	0.01441
$\langle 111 \rangle$ d	18.728	18.728	18.728	4.617	4.617	4.617	1052.2	0.000	42.635	0.00000	0.04052
$\langle 110 \rangle$ d	20.530	20.530	18.955	4.790	0.000	0.000	1200.6	0.827	15.299	0.00069	0.01274

investigate this, we have carried out NEB calculations, simulating pathways of rotation of an SIA dumbbell from a $[110]$ to a $[111]$ configuration in various metals. Figure 2 shows how the formation energy of a defect varies as a function of the reaction coordinate. We find a well defined minimum in all the three metals of group 6, corresponding to the orientation of the axis of the defect intermediate between the $[110]$ and $[111]$ directions. No minimum is found in bcc metals of group 5, where the curve is monotonic, as illustrated by the curve for niobium, which in the periodic table occupies a position next to molybdenum.

The intermediate between $[110]$ and $[111]$ configuration of the defect is stabilized by electronic chemical bonding effects and not by the effects of elastic interaction between periodically translated images of defects associated with the use of periodic boundary conditions. To prove this, we have computed the energy of elastic interaction E_{el}^{corr} following Refs. [13,33,34] and plotted it as a function of the NEB reaction coordinate in Fig. 3. The elastic correction varies monotonically as a function of the reaction coordinate, and the shape of the curve in Fig. 3 exhibits no correlation with the variation of the formation energy of defects shown in Fig. 2.

From the NEB calculations we took the lowest energy image and performed further ionic relaxation. In all the group 6 metals, the defect relaxed into a $\langle 11\xi \rangle$ dumbbell with the formation energy and orientation parameter ξ given in Table II. We find that ξ is an irrational number depending on the material and, where applicable, its magnetic state. The configuration that an SIA defect adopts in group 6 metals is different from a linear $\langle 111 \rangle$ configuration of the defect in vanadium, niobium, and tantalum [11]. It is also significantly different from the $\langle 110 \rangle$ dumbbell configuration that an SIA defect adopts in iron [16], where its structure is stabilized by magnetic effects. A sketch of the symmetry-broken $\langle 11\xi \rangle$ defect structure in Mo is shown in Fig. 4.

To verify that the observed symmetry-broken defect configuration is not an artifact of the finite simulation cell size, we have also carried out simulations using a larger cell containing $5 \times 5 \times 5$ bcc unit cells. The simulations were performed for

$\langle 11\xi \rangle$, $\langle 111 \rangle$, and $\langle 110 \rangle$ dumbbells. Their formation energies are given in Table III. Although the absolute values differ slightly from those given in Table II, the conclusion that the $\langle 11\xi \rangle$ dumbbell is the most stable SIA configuration, remains unchanged. We have also performed calculations for Mo using a noncubic simulation cell, containing $4 \times 4 \times 5$ bcc unit cells. The formation energy of a $\langle 11\xi \rangle$ SIA defect in this cell is 7.400 eV, which is close to the value of 7.399 eV found using a $4 \times 4 \times 4$ cubic simulation cell. This eliminates any remaining concern about the effect of the finite simulation cell size or its noncubic symmetry.

We note that in many DFT codes, including VASP, automatic crystal symmetry identification is applied to the simulation cell at the start of a calculation, to identify the irreducible k points. This accelerates calculations but constrains ionic relaxations to a particular crystal symmetry. If a lower energy configuration exists that does not comply with the initial symmetry of the simulation cell, a DFT calculation may not be able to find it, if the space group is defined at the start of the simulation. In this study, all the $\langle 11\xi \rangle$ dumbbell configurations were explored with no symmetry constraint applied. We find that the energy and structure that we identify as the ground state defect configuration, remains unchanged irrespectively of crystal symmetry constraints.

To understand the origin of symmetry breaking at the center of the defect, we have calculated the local density of electronic states (LDOS) projected onto one of the atoms at the center of $\langle 111 \rangle$ and $\langle 11\xi \rangle$ dumbbell configurations in Mo. LDOS plots for the two defect structures are shown in Fig. 5. To achieve sufficient accuracy of calculation of DOS, we used a $9 \times 9 \times 9$ k -point mesh. Calculations involved relaxed defect configurations simulated using a $4 \times 4 \times 4$ cell and $5 \times 5 \times 5$ k -point mesh. LDOS computed for a perfect bcc lattice 128 atom cell is shown for comparison. We see that the DOS for the two defect structures is only slightly higher at the Fermi energy (corresponding to the origin of the horizontal axis and indicated by a dashed vertical line), suggesting that the stabilization of the $\langle 11\xi \rangle$ dumbbell defect structure is not related to the changes in electronic structure near the Fermi energy ϵ_F . On the other hand, the

TABLE VI. Elements of dipole tensor P_{ij} (in eV units) and parameters π_1 , π_2 , and π_3 computed for $\langle 11\xi \rangle$, $\langle 111 \rangle$, and $\langle 110 \rangle$ dumbbells in Cr/NM. *Ab initio* calculations were performed using simulation cells containing $4 \times 4 \times 4$ bcc unit cells.

Cr/NM	P_{11}	P_{22}	P_{33}	P_{12}	P_{23}	P_{31}	π_1	π_2	π_3	π_2/π_1	π_3/π_1
$\langle 11\xi \rangle$ d	27.410	27.410	32.365	4.417	2.662	2.662	2533.8	8.181	22.455	0.00323	0.00886
$\langle 111 \rangle$ d	28.816	28.816	28.816	5.222	5.222	5.222	2491.0	0.000	54.543	0.00000	0.02190
$\langle 110 \rangle$ d	28.806	28.806	30.494	4.594	0.000	0.000	2587.6	0.950	14.071	0.00037	0.00544

TABLE VII. Elements of dipole tensor P_{ij} (in eV units) and parameters π_1 , π_2 , and π_3 computed for $\langle 11\xi \rangle$, $\langle 111 \rangle$, and $\langle 110 \rangle$ dumbbells in Mo. *Ab initio* calculations were performed using simulation cells containing $4 \times 4 \times 4$ bcc unit cells. Experimental values are taken from the study by Ehrhart [9] where Mo samples were exposed to electron irradiation at very low temperature.

Mo	P_{11}	P_{22}	P_{33}	P_{12}	P_{23}	P_{31}	π_1	π_2	π_3	π_2/π_1	π_3/π_1
$\langle 11\xi \rangle$ d	38.614	38.614	43.538	6.675	4.631	4.631	4861.4	8.082	58.301	0.00166	0.01441
$\langle 111 \rangle$ d	39.601	39.601	39.601	7.609	7.609	7.609	4704.6	0.000	115.789	0.00000	0.04052
$\langle 110 \rangle$ d	39.944	39.944	42.470	6.757	0.000	0.000	4990.4	2.128	30.438	0.00043	0.01274
Expt.										0.05 ± 0.02	0.04 ± 0.02

DOS for the $\langle 11\xi \rangle$ defect increases significantly at the lower edge of the band, explaining why the energy of the $\langle 11\xi \rangle$ dumbbell configuration is lower than the energy of the $\langle 111 \rangle$ configuration.

Figure 6 shows distances between successive atoms in atomic strings containing an extra atom in Cr/AFM, Cr/NM, Mo, and W, for a straight $\langle 111 \rangle$ defect configuration (top) and a symmetry-broken $\langle 11\xi \rangle$ configuration (bottom). The curves differ at the center of the defect, whereas a few lattice parameters away from the core the structure of the defects appear similar. The two atoms at the center of the symmetry-broken $\langle 11\xi \rangle$ dumbbell configuration are situated closer together than in a straight $\langle 111 \rangle$ dumbbell configuration.

In Fig. 7 we plot the Voronoi volume of atoms in the central $\langle 111 \rangle$ string, containing an extra atom. The Voronoi volume of an atom is computed using the Voro++ program [42]. Atoms at the center of a $\langle 11\xi \rangle$ dumbbell configuration occupy smaller volumes than in a straight $\langle 111 \rangle$ dumbbell configuration. In general, a symmetry-broken $\langle 11\xi \rangle$ dumbbell defect configuration appears more compact than a straight linear $\langle 111 \rangle$ configuration, and the difference is more pronounced in the case of Cr than in Mo or W.

A somewhat deeper insight into the nature of interatomic bonding at the core of defects can be gained from a comparison of charge difference plots shown in Figs. 8 and 9. The plot shown in Fig. 8 illustrates the effect of deformation of electron charge density due to the buckling of a straight linear $\langle 111 \rangle$ defect configuration. A precursor of symmetry breaking is already visible at the center of the $\langle 111 \rangle$ defect, where the symmetry of the charge density distribution is different from that of atoms in the surrounding perfect lattice.

IV. MIGRATION OF AN SIA DEFECT

Symmetry breaking also has implications for the migration of $\langle 11\xi \rangle$ SIA defects. The defects no longer migrate purely one dimensionally, retaining their straight $\langle 111 \rangle$

structure, as was assumed in Ref. [18]. It is instructive to compare the case with that of magnetic bcc iron, where an SIA defect adopts a $\langle 110 \rangle$ dumbbell configuration. In iron, a migrating SIA defect follows a three-dimensional translation-rotation pathway. DFT calculations show that a $[110]$ dumbbell transforms into a $[011]$ dumbbell located in an adjacent cell, and that the energy barrier for migration of the defect is close to 0.34 eV [16]. The predicted value is close to the experimentally measured migration energy of 0.30 eV and is compatible with the relatively high observed temperature of the onset of defect migration of 120 K [14].

Bearing in mind that the experimentally observed SIA defect migration temperatures in Cr, Mo, and W are 40, 35, and 27 K [14], respectively, we propose that a symmetry-broken SIA defect migrates through a translation-rotation pathway similar to that of a defect in Fe. A $\langle 11\xi \rangle$ dumbbell is a structure intermediate between a $\langle 111 \rangle$ and a $\langle 110 \rangle$ configuration. A possible migration pathway therefore might involve a transition from a $[11\xi]$ dumbbell structure to a $[\xi 11]$ dumbbell structure situated in an adjacent bcc unit cell. Symmetry considerations suggest that a $[11\xi]$ dumbbell can also jump to a $[1\xi 1]$ configuration. For any $\langle 11\xi \rangle$ dumbbell, there are two equivalent forward and two backward migration pathways along the $\langle 111 \rangle$ direction. A sketch illustrating the pathway of migration of a defect is shown in Fig. 10.

The pattern of migration above does not involve large nonelastic relaxation, and is compatible with the elastic after-effect experimental observations performed in Mo at 4.2 K [17]. Although there is some reorientation of the SIA during its migration, it is relatively small if one compares it with the translation-rotation migration of a $\langle 110 \rangle$ SIA in Fe. In addition, although every migration step is twice degenerate (a $[11\xi]$ defect can transform into adjacent $[\xi 11]$ or $[1\xi 1]$ configurations), each step involves a transformation similar to the one proposed by Jacques and Robrock [17] and

TABLE VIII. Elements of dipole tensor P_{ij} (in eV units) and parameters π_1 , π_2 , and π_3 computed for $\langle 11\xi \rangle$, $\langle 111 \rangle$, and $\langle 110 \rangle$ dumbbells in W. *Ab initio* calculations were performed using simulation cells containing $4 \times 4 \times 4$ bcc unit cells.

W	P_{11}	P_{22}	P_{33}	P_{12}	P_{23}	P_{31}	π_1	π_2	π_3	π_2/π_1	π_3/π_1
$\langle 11\xi \rangle$ d	50.921	50.921	57.883	11.925	9.136	9.136	8503.9	16.157	206.078	0.00190	0.01441
$\langle 111 \rangle$ d	52.754	52.754	52.754	13.128	13.128	13.128	8348.9	0.000	344.712	0.00000	0.04052
$\langle 110 \rangle$ d	52.557	52.557	56.960	11.277	0.000	0.000	8756.0	6.462	84.777	0.00074	0.01274

TABLE IX. Parameters used for the evaluation of atomic form factors, see Ref. [45] for further detail.

Element	a_1	$b_1 (\text{\AA}^2)$	a_2	$b_2 (\text{\AA}^2)$	a_3	$b_3 (\text{\AA}^2)$	a_4	$b_4 (\text{\AA}^2)$	c
Cr	10.6406	6.1038	7.3537	0.392	3.324	20.2626	1.4922	98.7399	1.1832
Mo	3.7025	0.2772	17.2356	1.0958	12.8876	11.004	3.7429	61.6584	4.3875
W	29.0818	1.72029	15.43	9.2259	14.4327	0.321703	5.11982	57.056	9.8875

illustrated schematically in Fig. 1. Still, the overall pattern of thermal migration of a defect is not two dimensional, but one dimensional, since *on average* a defect diffuses in a $\langle 111 \rangle$ direction closest to the orientation of the axis of the defect. This is also different from the case of a $\langle 110 \rangle$ dumbbell in Fe where it performs three-dimensional diffusion, involving eight equivalent hopping positions from a given equilibrium defect site, whereas a $\langle 11\xi \rangle$ dumbbell only has four such equivalent hopping positions.

NEB data for trajectories of migration of a defect from a $[11\xi]$ to a $[\xi 11]$ dumbbell configuration in group 6 metals are illustrated in Fig. 11. The corresponding values of elastic correction energy associated with the use of periodic boundary conditions are shown in Fig. 12. The barrier for defect migration is defined as the difference between the energies of the saddle and equilibrium points. The energy barrier for

migration of a defect in Cr/AFM is 0.052 eV, in Cr/NM it is 0.075 eV, in Mo it is 0.064 eV and in W it is 0.040 eV, as summarized in Table IV.

In the transition state approximation [20] the jump frequency equals

$$\nu = \nu_0 \exp(-E^m/k_B T), \tag{2}$$

where ν_0 is the attempt frequency. In transition state theory it is often assumed that the attempt frequency is proportional to the Debye frequency, and hence the Debye temperature θ of the material.

Using Fe as a benchmark, where $\theta_{\text{Fe}} = 470$ K [36], and assuming $\nu = 1 \text{ s}^{-1}$, we find $T_m = 124.3$ K, where the migration energy of a $\langle 110 \rangle$ dumbbell is taken as $E^m = 0.34$ eV [16]. This estimate compares well with the onset of migration

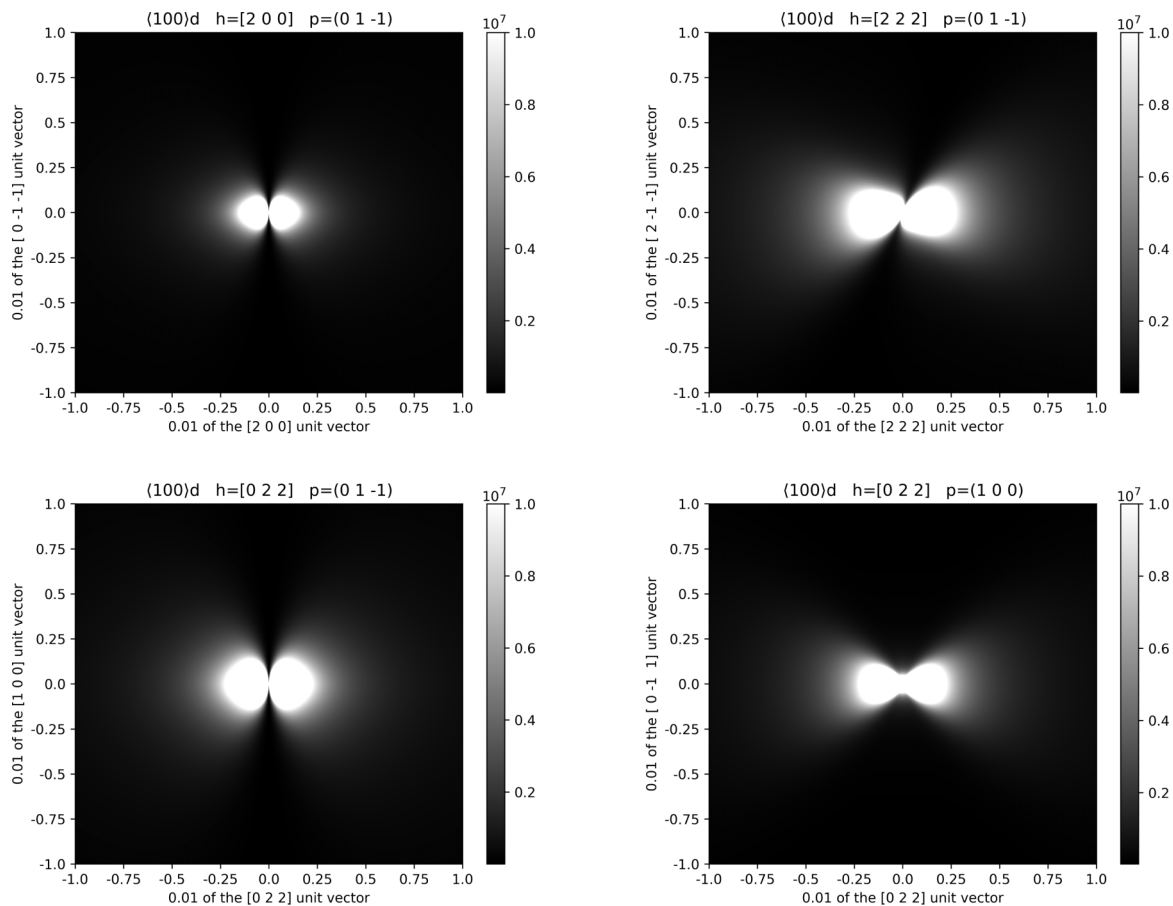


FIG. 13. Patterns of Huang diffuse scattering produced by an ensemble of randomly distributed and average over equivalent crystallographic orientations (100) dumbbells.

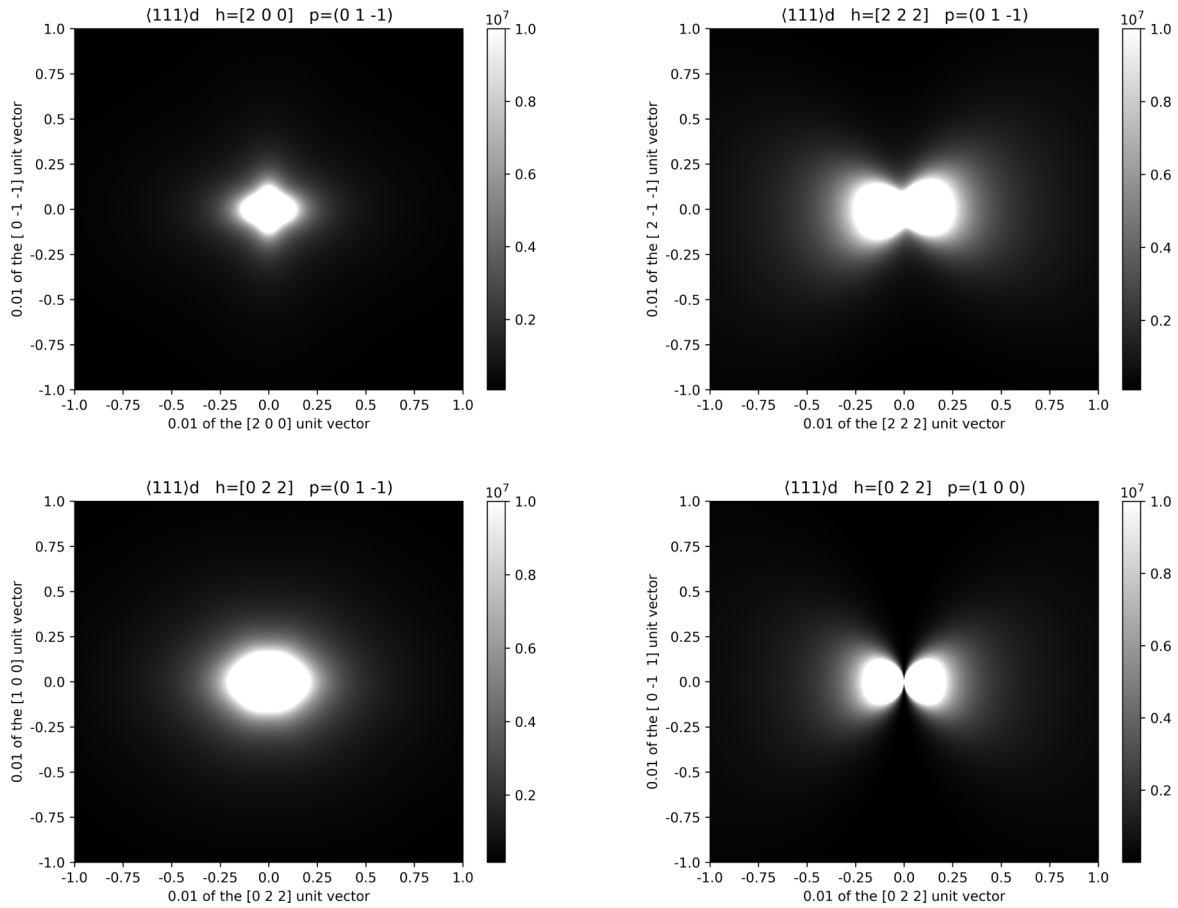


FIG. 14. Patterns of Huang diffuse scattering produced by randomly distributed and average over equivalent crystallographic orientations $\langle 111 \rangle$ dumbbells.

temperature of SIA defects of 120 K observed in experiment [14].

Similarly, using the Debye temperatures $\theta_{Cr} = 630$ K, $\theta_{Mo} = 450$ K, and $\theta_W = 400$ K taken from Ref. [36], we find the temperatures characterizing the onset of migration of SIA defects T_m^{SIA} of 18.7, 27.0, 23.5, and 14.7 K in Cr/AFM, Cr/NM, Mo, and W, respectively. These values compare well with the values derived from electron irradiated resistivity recovery experiments of 40, 35, and 27 K in Cr, Mo, and W [14]. The comparison is particularly informative given that the migration barrier for a *non*-symmetry-broken linear SIA defect in W is just 2 meV [19], and this corresponds to the onset of defect migration temperature of just 0.7 K, which is more than an order of magnitude lower than what is observed experimentally.

At higher temperatures, more complex migration pathways could be realized, involving for example a transformation of a $\langle 11\xi \rangle$ dumbbell into a $\langle 111 \rangle$ dumbbell, which then performs a purely one-dimensional migration step, followed by the formation of another symmetry-broken defect configuration. The difference between the formation energies of a $\langle 11\xi \rangle$ and a $\langle 111 \rangle$ SIA in Mo and W are 0.071 and 0.050 eV, respectively. These values are not too dissimilar from the migration energy associated with the transformation of an SIA defect from a $[11\xi]$ to a $[\xi 11]$ configuration.

V. INTERPRETATION OF HUANG X-RAY DIFFUSE SCATTERING PATTERNS

In the preceding sections we showed that an SIA defect in Cr, Mo, and W adopts a symmetry-broken $\langle 11\xi \rangle$ configuration, and its migration follows a translation-rotation pseudo-one-dimensional pathway that on average is collinear with a $\langle 111 \rangle$ crystallographic direction. This reconciles predictions derived from DFT calculations, resistivity recovery experiments, and observations of elastic after-effect. The remaining outstanding question concerns the interpretation of Huang x-ray diffuse scattering observations that, according to Ehrhart [9], indicate that an SIA defect in molybdenum adopts a $\langle 110 \rangle$ configuration.

If the concentration of point defects in a material is small, the symmetry of the long range strain field of such defects can be determined from Huang diffuse scattering patterns. Huang diffuse scattering intensities, produced by randomly distributed defects adopting all the possible symmetry-equivalent orientations, are characterized by the momentum transfer $\mathbf{K} = \mathbf{h} + \mathbf{q}$, where \mathbf{h} is a chosen reciprocal lattice vector. The scattered intensity distribution has the form [8]

$$S_H(\mathbf{K}) = N_{\text{def}} f_{\mathbf{h}}^2 \frac{h^2}{q^2} \frac{1}{V_{\text{uc}}^2} (\gamma_1 \pi_1 + \gamma_2 \pi_2 + \gamma_3 \pi_3). \quad (3)$$

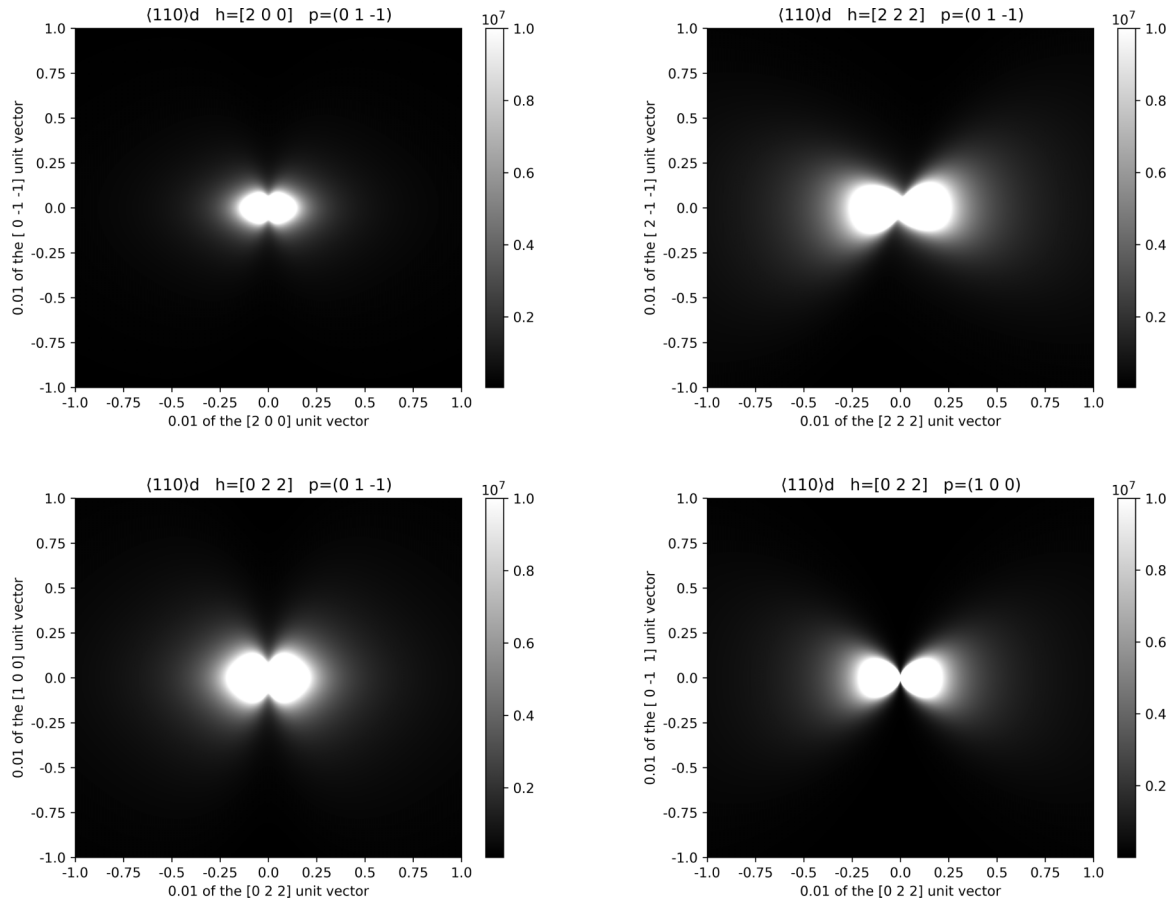


FIG. 15. Patterns of Huang diffuse scattering produced by randomly distributed and average over equivalent crystallographic orientations (110) dumbbells.

This formula, derived in the kinematic scattering approximation, shows that the cross section of scattering is proportional to the total number of defects N_{def} in the sample. In the above equation, $f_{\mathbf{h}}$ is the atomic scattering form factor, $V_{\text{uc}} = a_0^3$ is the volume of a unit cell, \mathbf{h} is a reciprocal lattice vector, and \mathbf{q} is a measure of deviation from the Bragg reflection. In Eq. (3) it is assumed that $|\mathbf{q}|$ is small in comparison with $|\mathbf{h}|$. Below, the values of \mathbf{K} , \mathbf{h} and \mathbf{q} are given in $2\pi/a_0$ units. Parameters γ_1 , γ_2 , and γ_3 depend on \mathbf{h} and \mathbf{q} , and also on the anisotropic elastic constants of the material, where

$$\gamma_1 = \frac{1}{3} \left(\sum_i T_{ii} \right)^2, \quad (4)$$

$$\gamma_2 = \frac{1}{3} \sum_{i>j} (T_{ii} - T_{jj})^2, \quad (5)$$

$$\gamma_3 = \frac{1}{2} \sum_{i>j} (T_{ij} + T_{ji})^2, \quad (6)$$

and

$$T_{ij} = \sum_l \hat{h}_l g_{li}(\hat{\mathbf{q}}) \hat{q}_j. \quad (7)$$

Introducing unit vectors $\hat{\mathbf{h}} = \mathbf{h}/h$ and $\hat{\mathbf{q}} = \mathbf{q}/q$, we write the matrix function $g_{li}(\hat{\mathbf{q}})$ as

$$g_{ij}(\hat{\mathbf{q}}) = \left(\sum_{kl} C_{ijkl} \hat{q}_k \hat{q}_l \right)^{-1}, \quad (8)$$

where C_{ijkl} is the elastic constant tensor. Parameters π_1 , π_2 , and π_3 depend only on the matrix elements of elastic dipole tensor P_{ij} of the defect, computed for a particular orientation, where

$$\pi_1 = \frac{1}{3} \left(\sum_i P_{ii} \right)^2, \quad (9)$$

$$\pi_2 = \frac{1}{6} \sum_{i>j} (P_{ii} - P_{jj})^2, \quad (10)$$

$$\pi_3 = \frac{2}{3} \sum_{i>j} P_{ij}^2. \quad (11)$$

Symmetry properties of π_1 , π_2 , and π_3 are such that the same values are obtained for any orientation of the defect that is related to its original orientation by symmetry operations pertinent to the underlying crystal lattice.

The dipole tensor of a localized defect object can be computed from macrostresses developing in a simulation box

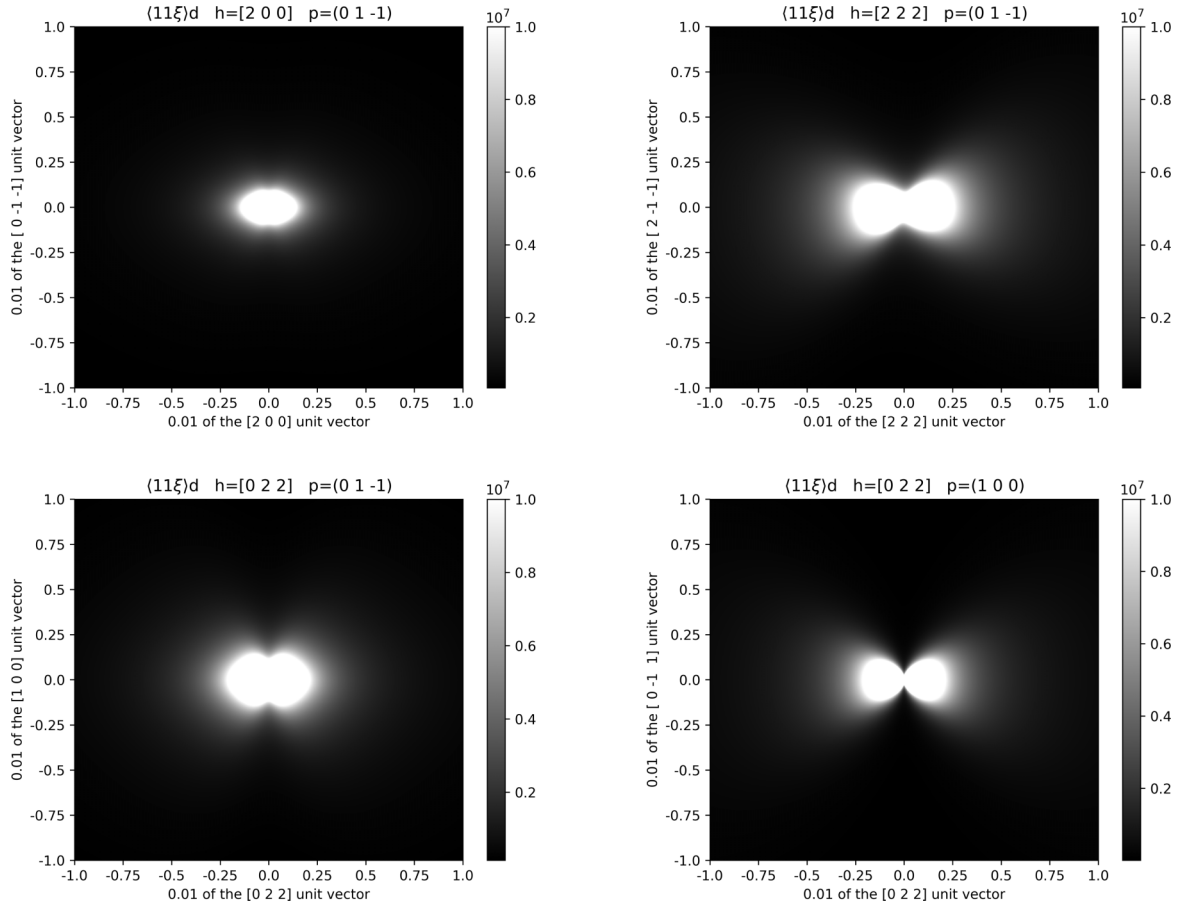


FIG. 16. Patterns of Huang diffuse scattering produced by randomly distributed and average over equivalent crystallographic orientations $\langle 11\xi \rangle$ SIA dumbbells.

due to the presence of a defect in it [33,34,43,44],

$$P_{ij} = V_{\text{cell}}(C_{ijkl}\epsilon_{kl}^{\text{app}} - \bar{\sigma}_{ij}), \quad (12)$$

where

$$\bar{\sigma}_{ij} = \frac{1}{V_{\text{cell}}} \int_{V_{\text{cell}}} \sigma_{ij} dV \quad (13)$$

is the average macroscopic stress in the simulation box, and $\epsilon_{kl}^{\text{app}}$ is the external applied stress. In this study, since we are using simulation boxes of the same size and shape as the reference perfect lattice, $\epsilon_{kl}^{\text{app}} = 0$. Dipole tensors P_{ij} of defects in Cr/AFM, Cr/NM, Mo, and W computed using Eq. (12) are given in Tables V to VIII. The tables also contain the computed values of parameters π_1 , π_2 , and π_3 .

An atomic scattering form factor may be approximated by a sum of Gaussian functions of the form [45]

$$f_{\kappa} = \sum_{i=1}^4 a_i \exp \left[-b_i \left(\frac{\kappa}{4\pi} \right)^2 \right] + c, \quad (14)$$

where a_i , b_i , and c for Cr, Mo, and W are listed in Table IX. The atomic form factor is a constant for a particular reflection \mathbf{h} .

Figures 13 to 16 show patterns of Huang diffuse scattering computed for randomly distributed $\langle 100 \rangle$, $\langle 111 \rangle$, $\langle 110 \rangle$, and $\langle 11\xi \rangle$ SIA defects in Mo. Since the scattering intensity is

linear in N_{def} , it is normalized to the number of defects in all the calculations. The cross section of Huang scattering $S_H(\mathbf{K})$ diverges at $q = 0$, and in numerical calculations we impose a maximum cutoff value of intensity of 1×10^7 . In choosing the Bragg reflections \mathbf{h} and the range of \mathbf{q} we follow Dederichs [8] and Ehrhart [9]. We simulate Huang scattering patterns for $\mathbf{h} = [200]$, $[222]$, and $[022]$, and take \mathbf{q} in the $\mathbf{p} = (01\bar{1})$ plane in reciprocal space. We also investigate the case $\mathbf{h} = [022]$ and $\mathbf{p} = (100)$.

In the case of a $\langle 100 \rangle$ dumbbell, we find zero intensity lines for $\mathbf{h} = [200]$ and $\mathbf{p} = (01\bar{1})$ and $\mathbf{h} = [022]$ and $\mathbf{p} = (01\bar{1})$. In the case of a $\langle 111 \rangle$ dumbbell, only the $\mathbf{h} = [022]$ and $\mathbf{p} = (100)$ plot exhibits a zero intensity line. In the case of $\langle 110 \rangle$ and $\langle 11\xi \rangle$ dumbbells, none of the plots exhibit zero intensity lines. In Fig. 17 we plot a Huang scattering pattern simulated over a smaller range of values of \mathbf{q} , for the better identification of zero intensity lines. All the patterns corresponding to the $\langle 100 \rangle$, $\langle 111 \rangle$, and $\langle 110 \rangle$ dumbbells are in agreement with calculations by Dederichs [8] and Ehrhart [9].

Our analysis shows that the key limiting factor in the studies by Ehrhart [9] was the fact that only the $\langle 100 \rangle$, $\langle 111 \rangle$, and $\langle 110 \rangle$ dumbbells were included as possible candidate structures of SIA defects. The computed Huang diffuse scattering patterns in Figs. 13–16 show that it is impossible to tell apart the scattering patterns corresponding to

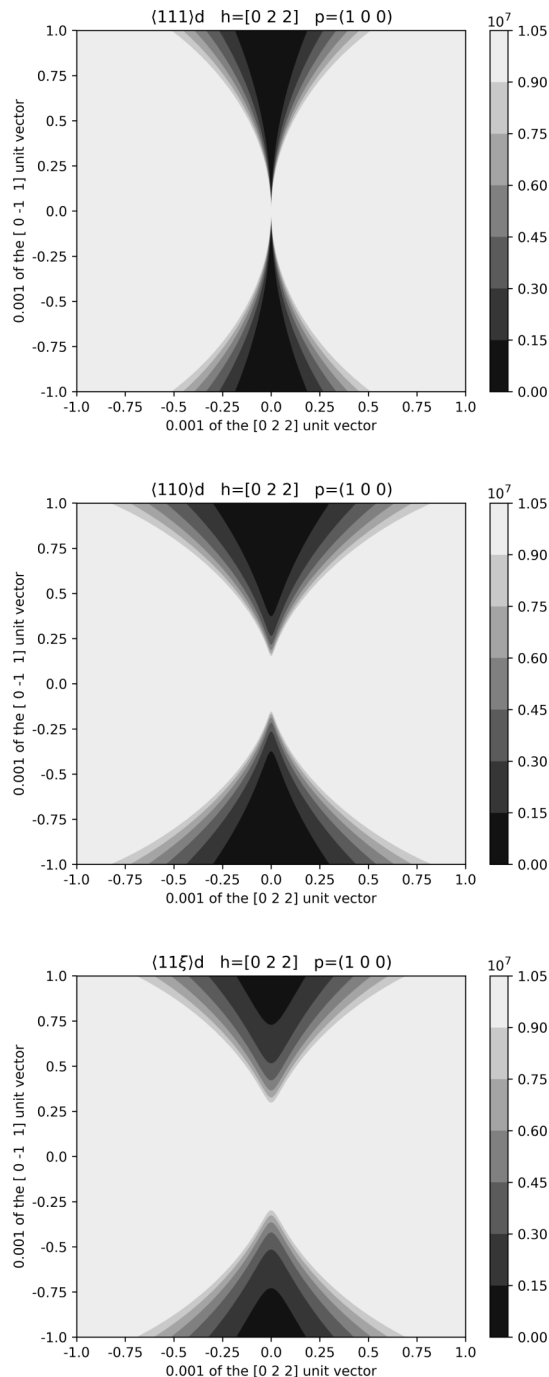


FIG. 17. Patterns of Huang diffuse scattering by $\langle 111 \rangle$, $\langle 110 \rangle$, and $\langle 11\xi \rangle$ randomly distributed and average over the equivalent crystallographic orientations dumbbell configurations computed for a $[022]$ reflection in the (100) plane in reciprocal space. Only the $\langle 111 \rangle$ dumbbell configurations produce zero intensity lines parallel to the $[0\bar{1}1]$ direction in reciprocal space.

the $\langle 110 \rangle$ and $\langle 11\xi \rangle$ defect structures. Bearing in mind the compelling evidence for the $\langle 11\xi \rangle$ dumbbell as the lowest energy SIA structure in molybdenum, we conclude that it is this structure that was mistakenly interpreted as the $\langle 110 \rangle$ defect structure in experiments by Ehrhart [9]. Indeed, none of the values of π_1 , π_2 , and π_3 vanish for either the $\langle 110 \rangle$ or $\langle 11\xi \rangle$ defect, which is the reason why in a Huang diffuse scattering experiment one cannot distinguish these two SIA configurations.

VI. CONCLUSION

We show that a symmetry-broken $\langle 11\xi \rangle$ dumbbell represents the most stable defect configuration of a self-interstitial atom defect in all the group 6 metals of the periodic table. Parameter ξ is an irrational number, depending on the material and its magnetic state. Defects migration follows a rotation-translation pathway, which on average appears similar to one-dimensional diffusion in a $\langle 111 \rangle$ crystallographic direction. Barriers for the migration of defects are significantly larger than those predicted by a purely one-dimensional migration model. They are 52 meV in antiferromagnetic Cr, 75 meV in nonmagnetic Cr, 64 meV in Mo, and 40 meV in W. These values correlate well with the temperatures characterizing the onset of migration of defects in various metals observed experimentally. Huang diffuse scattering patterns computed using the DFT data show that on the basis of experimental data Ref. [9] and other studies it is not possible to distinguish between $\langle 110 \rangle$ and $\langle 11\xi \rangle$ configurations, and conclusively identify a defect structure from observations. Defect configurations predicted by *ab initio* simulations in group 6 metals resolve the controversy associated with the interpretation of experimental data, and reconcile observations with fundamental theory.

ACKNOWLEDGMENTS

We are grateful to Pär Olsson for a fruitful discussion. This work has been carried out within the framework of the EUROfusion Consortium and has received funding from the Euratom research and training programme 2014-2018 and 2019-2020 under grant agreement No. 633053 and from the RCUK Energy Programme (Grant No. EP/P012450/1). To obtain further information on the data and models underlying this paper please contact PublicationsManager@ukaea.uk. The views and opinions expressed herein do not necessarily reflect those of the European Commission. We also acknowledge EUROfusion for the provision of access to the Marconi supercomputer facility at CINECA in Bologna, Italy.

- [1] E. A. Little and D. A. Stow, Void swelling in iron and ferritic steels: II. An experimental survey of materials irradiated in a fast reactor, *J. Nucl. Mater.* **87**, 25 (1979).
 [2] V. K. Kharchenko and V. V. Bukhanovskii, High-temperature strength of refractory metals, alloys and

composite materials based on them. Part 1. Tungsten, its alloys, and composites, *Strength Mater.* **44**, 512 (2012).

- [3] V. K. Kharchenko and V. V. Bukhanovskii, High-temperature strength of refractory metals, alloys and composite

- materials based on them. Part 2. Molybdenum and niobium alloys, *Strength Mater.* **44**, 617 (2012).
- [4] D. Y. Park, Y. J. Oh, Y. S. Kwon, S. T. Lim, and S. J. Park, Development of non-eroding rocket nozzle throat for ultra-high temperature environment, *Int. J. Refract. Met. Hard Mater.* **42**, 205 (2014).
- [5] D. Stork, P. Agostini, J.-L. Boutard, D. Buckthorpe, E. Diegele, S. L. Dudarev, C. English, G. Federici, M. R. Gilbert, S. Gonzalez, A. Ibarra, C. Linsmeier, A. L. Puma, G. Marbach, L. W. Packer, B. Raj, M. Rieth, M. Q. Tran, D. J. Ward, and S. J. Zinkle, Materials R&D for a timely DEMO: Key findings and recommendations of the EU Roadmap Materials Assessment Group, *Fusion Eng. Des.* **89**, 1586 (2014), Proceedings of the 11th International Symposium on Fusion Nuclear Technology-11 (ISFNT-11) Barcelona, Spain, 15–20 September 2013.
- [6] D. Stork, P. Agostini, J. L. Boutard, D. Buckthorpe, E. Diegele, S. L. Dudarev, C. English, G. Federici, M. R. Gilbert, S. Gonzalez, A. Ibarra, Ch. Linsmeier, A. L. Puma, G. Marbach, P. F. Morris, L. W. Packer, B. Raj, M. Rieth, M. Q. Tran, D. J. Ward, and S. J. Zinkle, Developing structural, high-heat flux and plasma facing materials for a near-term DEMO fusion power plant: The EU assessment, *J. Nucl. Mater.* **455**, 277 (2014), Proceedings of the 16th International Conference on Fusion Reactor Materials (ICFRM-16).
- [7] M. Durrand-Charre, *Microstructure of Steels and Cast Irons* (Springer, Berlin, 2003).
- [8] P. H. Dederichs, The theory of diffuse x-ray scattering and its application to the study of point defects and their clusters, *J. Phys. F* **3**, 471 (1973).
- [9] P. Ehrhart, The configuration of atomic defects as determined from scattering studies, *J. Nucl. Mater.* **69-70**, 200 (1978).
- [10] P. Ehrhart, K. H. Robrock, and H. R. Schober, basic defects in metals, in *Physics of Radiation Defects in Crystals*, edited by R. A. Johnson and A. N. Orlov (Elsevier, Amsterdam, 1986), pp. 7–115.
- [11] D. Nguyen-Manh, A. P. Horsfield, and S. L. Dudarev, Self-interstitial atom defects in bcc transition metals: Group-specific trends, *Phys. Rev. B* **73**, 020101(R) (2006).
- [12] P. M. Derlet, D. Nguyen-Manh, and S. L. Dudarev, Multi-scale modeling of crowdion and vacancy defects in body-centered-cubic transition metals, *Phys. Rev. B* **76**, 054107 (2007).
- [13] P.-W. Ma and S. L. Dudarev, Universality of point defect structure in body-centered cubic metals, *Phys. Rev. Mater.* **3**, 013605 (2019).
- [14] P. Ehrhart, P. Jung, H. Schultz, and H. Ullmaier, in *Landolt-Börnstein - Group III Condensed Matter Volume 25: "Atomic Defects in Metals"*, edited by H. Ullmaier (Springer, Berlin, 1991).
- [15] H. Schultz, Defect parameters of b.c.c. metals: Group-specific trends, *Mater. Sci. Eng. A* **141**, 149 (1991).
- [16] C.-C. Fu, F. Willaime, and P. Ordejón, Stability and Mobility of Mono- and Di-Interstitials in α -Fe, *Phys. Rev. Lett.* **92**, 175503 (2004).
- [17] H. Jacques, and K.-H. Robrock, Elastic after effect studies of molybdenum after electron irradiation at 4.7 K, *J. Phys. Colloques* **42**, C5-723 (1981).
- [18] S. P. Fitzgerald and D. Nguyen-Manh, Peierls Potential for Crowdions in the bcc Transition Metals, *Phys. Rev. Lett.* **101**, 115504 (2008).
- [19] T. D. Swinburne, P.-W. Ma, and S. L. Dudarev, Low temperature diffusivity of self-interstitial defects in tungsten, *New J. Phys.* **19**, 073024 (2017).
- [20] G. H. Vineyard, Frequency factors and isotope effects in solid state rate processes, *J. Phys. Chem. Solids* **3**, 121 (1957).
- [21] P. Olsson, *Ab initio* study of interstitial migration in Fe–Cr alloys, *J. Nucl. Mater.* **386-388**, 86 (2009).
- [22] S. Han, L. A. Zepeda-Ruiz, G. J. Ackland, R. Car, and D. J. Srolovitz, Self-interstitials in V and Mo, *Phys. Rev. B* **66**, 220101(R) (2002).
- [23] L. Ventelon, F. Willaime, C.-C. Fu, M. Heran, and I. Ginoux, *Ab initio* investigation of radiation defects in tungsten: Structure of self-interstitials and specificity of di-vacancies compared to other bcc transition metals, *J. Nucl. Mater.* **425**, 16 (2012).
- [24] L. Gharraee and P. Erhart, A first-principles investigation of interstitial defects in dilute tungsten alloys, *J. Nucl. Mater.* **467**, 448 (2015).
- [25] G. Kresse and J. Hafner, *Ab initio* molecular dynamics for liquid metals, *Phys. Rev. B* **47**, 558 (1993).
- [26] G. Kresse and J. Hafner, *Ab initio* molecular-dynamics simulation of the liquid-metal–amorphous-semiconductor transition in germanium, *Phys. Rev. B* **49**, 14251 (1994).
- [27] G. Kresse and J. Furthmüller, Efficiency of *ab initio* total energy calculations for metals and semiconductors using a plane-wave basis set, *Comput. Mater. Sci.* **6**, 15 (1996).
- [28] G. Kresse and J. Furthmüller, Efficient iterative schemes for *ab initio* total-energy calculations using a plane-wave basis set, *Phys. Rev. B* **54**, 11169 (1996).
- [29] J. P. Perdew, K. Burke, and M. Ernzerhof, Generalized Gradient Approximation Made Simple, *Phys. Rev. Lett.* **77**, 3865 (1996).
- [30] J. P. Perdew, K. Burke, and M. Ernzerhof, Generalized Gradient Approximation Made Simple [Phys. Rev. Lett. **77**, 3865 (1996)], *Phys. Rev. Lett.* **78**, 1396 (1997).
- [31] R. Hafner, D. Spišák, R. Lorenz, and J. Hafner, Magnetic ground state of Cr in density-functional theory, *Phys. Rev. B* **65**, 184432 (2002).
- [32] S. Cottenier, B. De Vries, J. Meersschant, and M. Rots, What density-functional theory can tell us about the spin-density wave in Cr, *J. Phys.: Condens. Matter* **14**, 3275 (2002).
- [33] C. Varvenne, F. Bruneval, M.-C. Marinica, and E. Clouet, Point defect modeling in materials: Coupling *ab initio* and elasticity approaches, *Phys. Rev. B* **88**, 134102 (2013).
- [34] S. L. Dudarev and P.-W. Ma, Elastic fields, dipole tensors, and interaction between self-interstitial atom defects in bcc transition metals, *Phys. Rev. Mater.* **2**, 033602 (2018).
- [35] Y. Le Page and P. Saxe, Symmetry-general least-squares extraction of elastic data for strained materials from *ab initio* calculations of stress, *Phys. Rev. B* **65**, 104104 (2002).
- [36] C. Kittel, *Introduction to Solid State Physics*, 8th ed. (John Wiley & Sons, New York, 2004).
- [37] S. B. Palmer and E. W. Lee, The elastic constants of chromium, *Philos. Mag.* **24**, 311 (1971).
- [38] M. W. Finnis and J. E. Sinclair, A simple empirical N-body potential for transition metals, *Philos. Mag. A* **50**, 45 (1984).
- [39] G. Mills, H. Jónsson, and G. K. Schenter, Reversible work transition state theory: Application to dissociative adsorption of hydrogen, *Surf. Sci.* **324**, 305 (1995).
- [40] H. Jónsson, G. Mills, and K. W. Jacobsen, Nudged elastic band method for finding minimum energy paths of transitions, in

- Classical and Quantum Dynamics in Condensed Phase Simulations* (World Scientific, Singapore, 1998), pp. 385–404.
- [41] P. Olsson, C. Domain, and J. Wallenius, *Ab initio* study of Cr interactions with point defects in bcc Fe, *Phys. Rev. B* **75**, 014110 (2007).
- [42] C. H. Rycroft, VORO++: A three-dimensional Voronoi cell library in C++, *Chaos* **19**, 041111 (2009).
- [43] E. Clouet, S. Garruchet, H. Nguyen, M. Perez, and C. S. Becquart, Dislocation interaction with C in α -Fe: A comparison between atomic simulations and elasticity theory, *Acta Mater.* **56**, 3450 (2008).
- [44] C. Varvenne and E. Clouet, Elastic dipoles of point defects from atomistic simulations, *Phys. Rev. B* **96**, 224103 (2017).
- [45] P. J. Brown, A. G. Fox, E. N. Maslen, M. A. O’Keefe, and B. T. M. Willis, Intensity of diffracted intensities, *Int. Tables Crystallogr. C*, 554 (2006).